SO_2, silicate clouds, but no CH_4 detected in a warm Neptune with JWST MIRI

Achrène Dyrek[1,⋆,†], Michiel Min[2,†], Leen Decin[3,†], Jeroen Bouwman[4], Nicolas Crouzet[5], Paul Mollière[4], Pierre-Olivier Lagage[6], Thomas Konings[3], Pascal Tremblin[7], Manuel Güdel[8,4,9], John Pye[10], Rens Waters[11,12,2], Thomas Henning[4], Bart Vandenbussche[3], Francisco Ardevol Martinez[13,2,14,15], Ioannis Argyriou[3], Elsa Ducrot[6], Linus Heinke[3,14,15], Gwenael Van Looveren[8], Olivier Absil[16], David Barrado[17], Pierre Baudoz[18], Anthony Boccaletti[18], Christophe Cossou[19], Alain Coulais[6,20], Billy Edwards[2], René Gastaud[19], Alistair Glasse[21], Adrian Glauser[9], Thomas P. Greene[22], Sarah Kendrew[23], Oliver Krause[4], Fred Lahuis[2], Michael Mueller[13], Goran Olofsson[24], Polychronis Patapis[9], Daniel Rouan[17], Pierre Royer[3], Silvia Scheithauer[4], Ingo Waldmann[25], Niall Whiteford[26], Luis Colina[17], Ewine van Dishoeck[5], Göran Ostlin[27], Tom P. Ray[28], Gillian Wright[29]

[†]Equal contribution is indicated by shared first-authorship.
[⋆]Corresponding author(s). Email(s): achrene.dyrek@cea.fr.
All author affiliations are listed at the end of the main paper.

Supplementary information

1. Data non-linearity correction

The adopted readout pattern for all JWST instruments, including those of the MIRI instrument, is the so-called `MULTIACCUM` readout pattern. The MIRI pixels are read non-destructively (charges are read but not reset) at a constant rate until a final read followed by two resets to clear the accumulated charges. An integration thus consists of a number of samples of the accumulating detector signal, resulting in a ramp, that, when fit, yields a measure of the flux per pixel. For a detailed discussion of the MIRI focal plane arrays and read out patterns we refer to ref. [1].

The MIRI detector ramps show several non-ideal behaviours influencing the slope derivation and thus the flux estimates. We refer to ref. [2] for a review of all detector effects influencing the sampling of the detector ramps and their mitigation in the JWST data reduction pipeline. The two main non-linearity effects which are important for transit observations are the reset switch charge decay[2] and the debiasing effect[2,3]. While the former affects mainly the first view reads of the detector ramps, and can be mitigated by not using the affected reads when determining the slope of the detector ramps, the latter needs to be corrected before the slope of the detector ramps can be correctly measured.

For a detailed discussion on the detector voltage debiasing and related effects, see ref. [3]. In brief, a detector circuit as used in MIRI can be seen as a resistor-capacitor circuit. Charge accumulation at the integration capacitors reduces the net bias voltage, which in turn leads to a lower response of the detector as it causes the width of the depletion region to shrink below the active layer width, and a smaller fraction of the produced photoelectrons are guided to the pixels. The diffusion of photo-excited electrons in the undepleted region of a (near) saturated pixel to the depleted region at neighbouring pixels – dubbed the brighter-fatter effect[3] – is not substantial in the WASP-107b data, as the maximum observed signal level of the detector ramps remains well below the saturation limit. Therefore we ignored the latter effect in our analysis, and focused on correcting the main detector ramp non-linearity due to debiasing.

The standard correction for the non-linearity of the detector ramps due to the debiasing effect, implemented in the `linearity` step of the JWST data reduction pipeline, is derived by fitting a cubic polynomial to the detector ramps of dedicated calibration data, and using the linear term as an estimate of the linearised signal of the detector ramp. A functional relation is then determined between linearised signal and observed signal using a fourth-order polynomial. The polynomial coefficients from this latter fit are stored in the CRDS calibration file for the `linearity` pipeline step. Note that the standard linearity correction implements an identical correction for all detector pixels in the MIRI/LRS subarray.

To test the default linearity correction (pmap version 1030), we checked the behaviour of the detector ramps by creating pair-wise differences of the readouts (frames). In case of a perfect linear ramp, the pair-wise differences of a detector ramp for a single detector pixel should have a constant value. The left column of Suppl. Inf. Fig. 1 show the pair-wise differences of the uncalibrated data (`uncal` data product), clearly showing non-constant values for those pixels receiving the highest photon flux. Note that the slope change of the first few differences is dominated by the RSCD, and the last pair by the last-frame effect. Applying the default linearity correction substantially improves the linearity of the ramps but a slope can still be seen when plotting the pair-wise differences in the second column of Suppl. Inf. Fig. 1, indicating that the default correction is not yet optimal. As non-linearity effects can have a substantial impact on the derived transit depth, we derived an alternative linearity correction based on the data itself. We fitted the following function to the detector ramps

$$\mathrm{S_{ij}}(t) = a_{ij,0} + \tau_{ik,1} \cdot a_{ij,1} \cdot \left(1 - \mathrm{e}^{\frac{-t}{\tau_{ij,1}}}\right) - \tau_{ij,2} \cdot a_{ij,2} \cdot \mathrm{e}^{\frac{-t}{\tau_{ij,2}}}$$

$$i \in \{0, \ldots, 415\}, \quad j \in \{0, \ldots, 72\}, \quad 0 \leq t \leq \mathrm{T_{int}}$$

In this equation, t is the time between 0 and the duration of a single integration $\mathrm{T_{int}}$. The first term represents the debiasing effect, with $a_{ij,0}$ the reset level for a single pixel with detector row index i and column index j, $a_{ij,1}$ and $\tau_{ik,1}$ the linearised slope of the detector ramp and the time constant of the debiasing effect, respectively. The second term models the RSCD effects with $a_{ij,2}$ and $\tau_{ij,2}$ the amplitude and time constant for the estimate of the RSCD effect. Though we will not use the fitted contribution of the RSCD effect in this study, we included the term in the fit to ensure we obtained an unbiased estimate of the debiasing effect. Using this model, we fitted the detector ramps after applying the `reset` pipeline step, for all integrations after the transit. Using the fitted estimate of the linearised signal, we followed the procedure described in ref. [2] to derive a custom non-linearity correction used in the `linearity` pipeline step. The right column of Suppl. Inf. Fig. 1 shows the slope estimates of the linearised ramps using our custom non-linearity procedure. Comparing this to the linearised ramps using the standard calibration, one can observe a substantial improvement in the linearity of the ramps for the brighter pixels. For those detector pixels having a low signal, no differences can be observed. This is expected as the detector ramps for those pixels are expected to be (near) linear.

Another test to check the non-linearity correction of the detector ramps is to look at the full width half maximum (FWHM) of the spectral trace. As the central detector pixels in the spectral trace see a stronger signal, they will be subject to a stronger non-linearity, leading to a broadening of the point spread function of the individual readouts of the detector ramps during an integration [3]. Suppl. Inf. Fig. 2 shows our estimates of the FWHM of the spectral trace for different detector ramp frame difference pairs. The left panels show the average FWHM of the spectral trace for frame difference pairs 5 to 10, which are the first samples not substantially influenced by the RSCD effects, and the frame difference pairs 34 to 38, respectively. The data calibrated using the standard calibration (top left panel) clearly shows a broadening of the point spread function (PSF) during an integration. The custom calibrated data, however, shows no such effect (lower left panels). The right panels of Suppl. Inf. Fig. 2 show the average FWHM as a function of frame difference pair for the detector rows 382 to 386, which sample the shortest wavelengths and receive the highest photon flux from the target. Again, the detector data calibrated with the standard calibration shows a broadening of the PSF during the sampling up the ramp (top right panel) while no such effect can be observed for the data calibrated with our custom calibration (lower right panel). The shaded grey regions in the right panels indicate the data not used in the final determination of the slopes of the detector ramps, as those points are strongly affected by the RSCD and last-frame effects.

Finally, Suppl. Inf. Fig. 3 shows the FWHM of the brightest pixels in time. As one can clearly see from this figure, the data calibrated using the standard CRDS calibration clearly shows a drop of the derived FWHM during the transit. The drop in the observed signal during the transit of about 2% is clearly enough to have a measurable effect on the photometric signal in case the non-linearity of the detector ramps is not properly corrected. Applying our custom calibration for this dataset, no significant effect of the transit on the FWHM estimate can be observed.

2. HST data reduction

A transit of WASP-107b was observed on June 5–6, 2017 with the Wide Field Camera 3 (WFC3) instrument onboard the *Hubble Space Telescope* (HST) using the 1.41 μm Grism (G141). The data was obtained as part of the general observer program 14915 (P.I. L. Kreidberg). We refer to ref. [4] for details on the observations and the initial data analysis. We performed an independent calibration and light curve fitting of the HST data using the `CASCADe` package. For details on the use of `CASCADe` on HST data, see ref. [5]. We ran `CASCADe` using the same orbital and stellar parameters as used for the analysis of the JWST MIRI light curve data (see Methods), with the

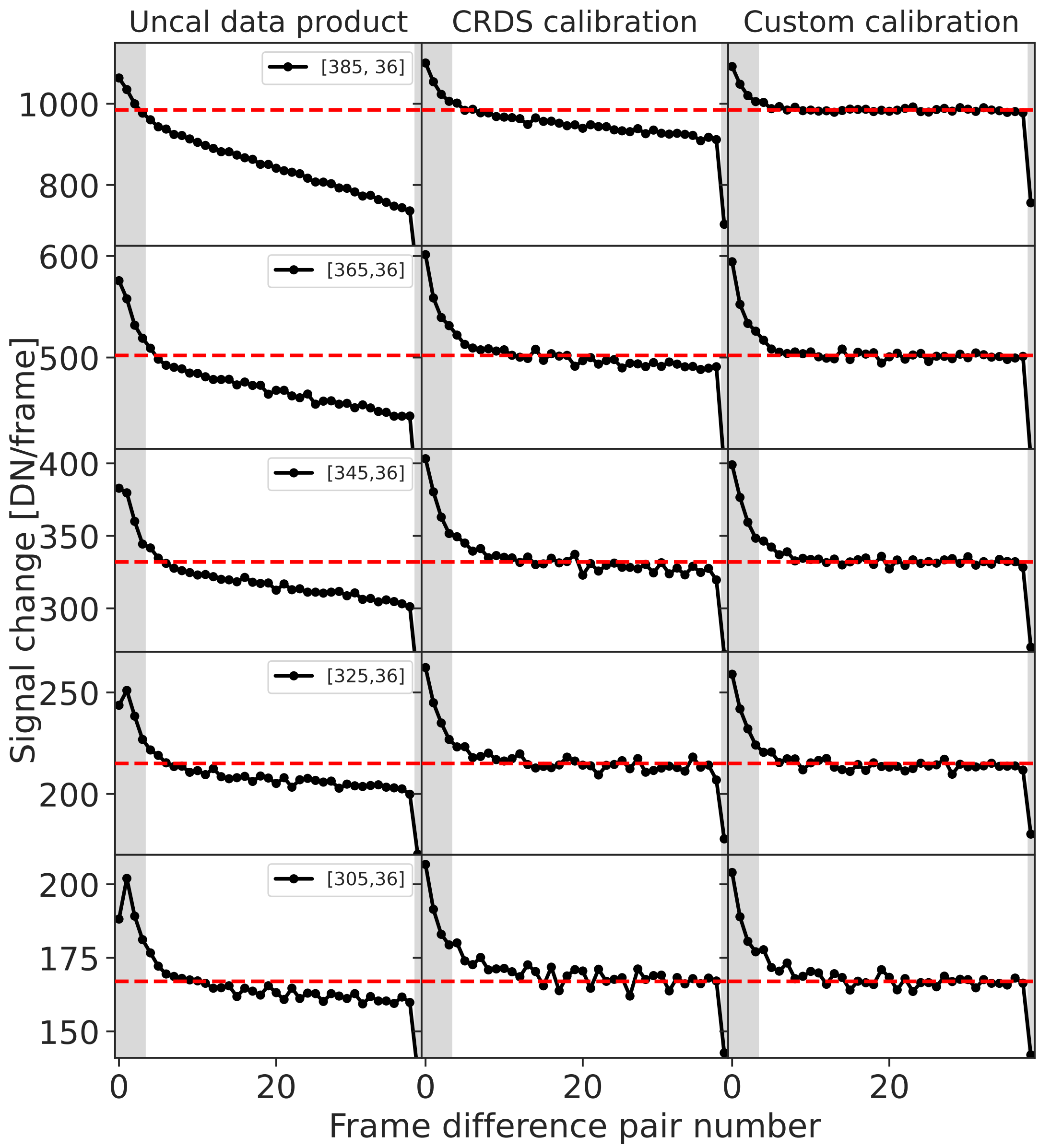

Suppl. Inf. – Figure 1: **Linearity of the detector ramps.** Shown are the pair-wise differences of the samples of the detector ramps for a number of detector pixels. From left to right are shown the ramp gradients for the `uncal` data product, the standard `reset`, `dark` and `linearise` processed data using the calibration files from CRDS with pmap version 1030, and the data product using a custom calibration for the `linearise` and `dark` calibration steps. From top to bottom are shown the data for 5 detector pixels corresponding to the maximum signal in the spectral trace of WASP-107b at different wavelengths. The pixel indices are indicated in the legends shown in the left column. The shaded grey regions indicate the data not used in the final determination of the slopes of the detector ramps. The red dashed lines are plotted to guide the eye and represent the average linear slope after applying our custom calibration.

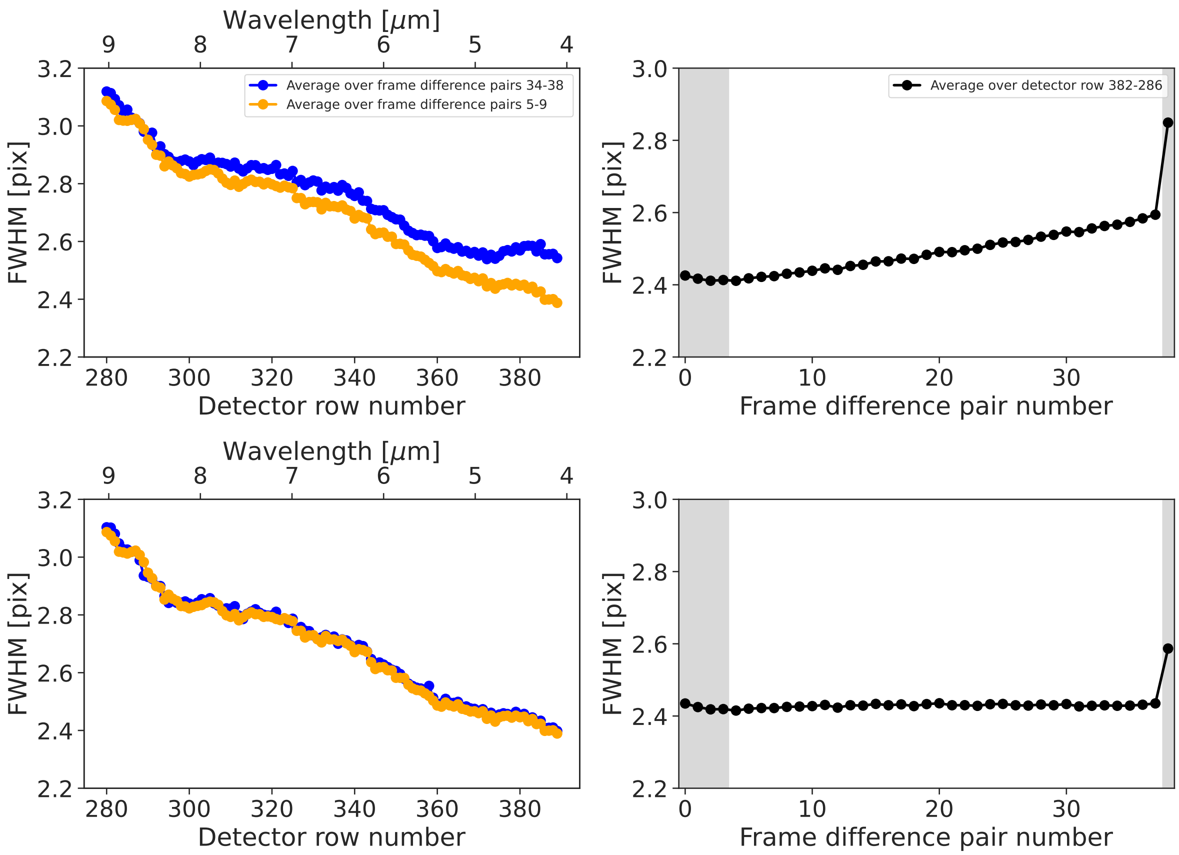

Suppl. Inf. – Figure 2: **FWHM estimates of the spectral trace for different detector ramp frames.** The top panels show the results for the standard calibrated detector ramps while the bottom panels show the results from our custom calibrated data. The left panels show the average FWHM of the spectral trace for detector rows 280 to 390, for frame difference pairs 5 to 10, and 34 to 38, respectively. The right panels show the average FWHM as a function of frame difference pair number for detector rows with the highest signal. The shaded grey regions in the right panels indicate the data not used in the final determination of the slopes of the detector ramps.

exception of the ephemeris, for which we used the value published in ref. [6]. This latter value gives a mid transit time within 28 s of the value derived by ref. [4]. We choose to use the value of ref. [6] as it resulted in slightly lower residuals after subtracting the best fit light curve model.

Before fitting the spectral light curve data, we binned the original spectral resolution of the HST/WFC3 data to a uniform wavelength grid with a spectral bin width of 0.00757μm. Of the first HST orbit, the first 6 spatial scans were not used in our analysis as they showed a very strong initial drift. For the systematics model (see ref. [5] for details), the additional regression parameters were the time variable and the trace position. The derived transit spectrum is plotted in the top panel of Fig. 4 (blue squares). We derived a band-averaged transit depth of 20448±79 ppm, consistent within 1σ of the transit depth derived from the JWST MIRI observations. The errors in the transit

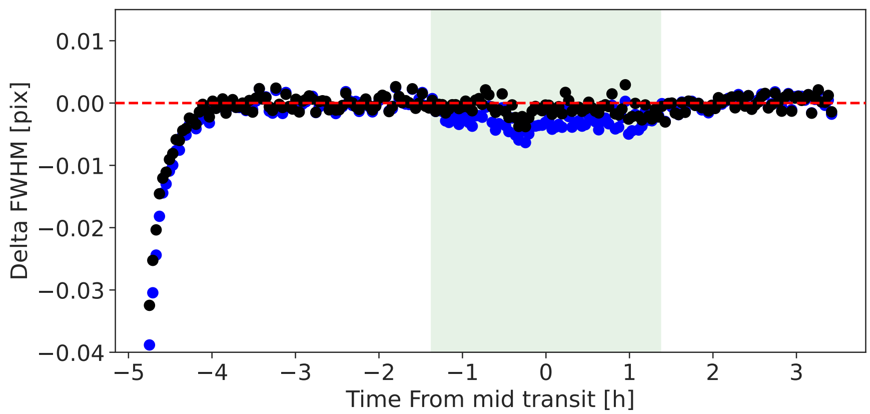

Suppl. Inf. – Figure 3: **Mean FWHM of the spectral trace for the detector rows 380 to 390.** The blue data points show the results after applying the standard calibration from CRDS, the black data point the results after using our custom non-linearity correction. To show the non-linearity effects more clearly, each data point represents an average of 22 integrations. The red dashed line is plotted to guide the eye and represents zero variations. The shaded green area indicates the time window where the transit occurs.

spectrum and band-averaged depth were estimated by performing a bootstrap analysis. For the retrieval analysis, we binned the spectrum to a slightly lower spectral resolution, with a spectral bin width of about 0.02 μm to increase the signal-to-noise ratio per spectral channel and to ensure that each spectral bin is independent. A comparison of the spectrum derived using the `CASCADe` package to the previous published spectrum of ref. [4] can be seen in the lower panel of Fig. 4. Both spectra are in excellent agreement with each other. The band-averaged transit depth of ref. [4] is 145 ppm, less than 2σ, larger than the averaged depth we derived. This difference is consistent with the quoted error bars and can easily be explained by the large systematics and sparse time sampling of the data, in combination with the different methods used to fit the baselines of the spectral light curves.

3. UV and X-ray data reduction setup

3.1. NUV emission

Contemporaneously with the JWST observations, from 2023 January 5 to 29, *Swift* conducted a 'Target of Opportunity' (ToO) observing campaign (Target Id. 15428) for WASP-107, with the UVOT[7] as the primary instrument, and utilising the uvm2 filter to optimise the waveband definition and avoid redward 'leaks' present in uvw2[8]. The uvm2 filter has a central wavelength of 2246 Å and a FWHM of 498 Å[9]. The observing campaign consisted of 13 *observation segments* comprising a total of 20 *snapshots* (i.e. continuous exposure periods). Each segment was typically $\sim 1.5 - 2$ ks in duration; with snapshots ranging from the full segment length down to ~ 500 s. All

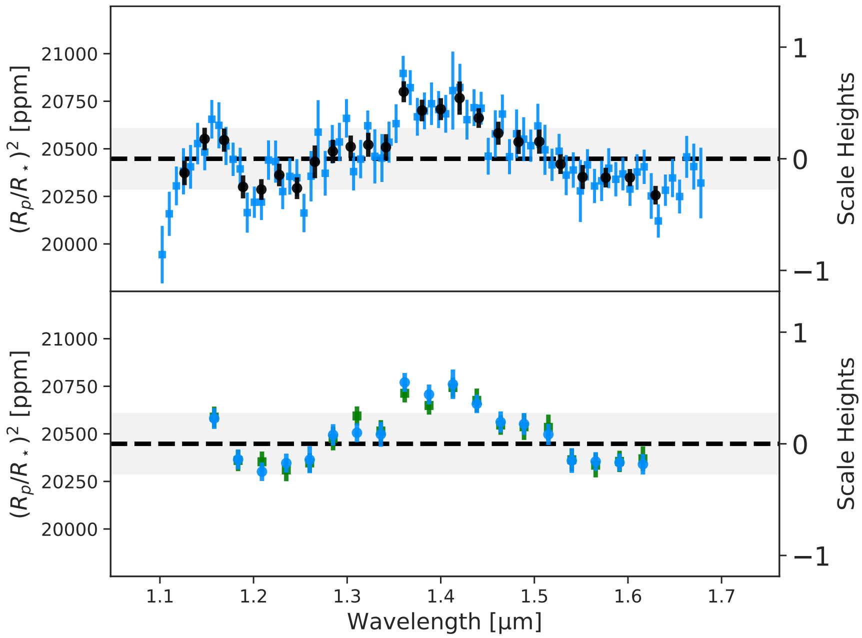

Suppl. Inf. – Figure 4: **HST/WFC3 transmission spectrum of WASP-107b.** The top panel shows the transmission spectrum derived using the `CASCADe` package (blue squares) together with a slightly lower resolution version of the same spectrum used in the retrieval analysis (black dots). The lower panel shows the comparison between the spectrum derived by ref. [4] (green squares) and the `CASCADe` spectrum (blue dots), binned to the published wavelength resolution of ref. [4]. In both panels, the band averaged transit depth is indicated by the dashed vertical line. The shaded grey area represents the 95 % confidence interval of the mean transit depth. The right y-axis gives the planetary spectrum in units of atmospheric scale height of the planetary atmosphere assuming it to be hydrogen dominated. In the lower panel, the ref. [4] spectrum was shifted downwards by 145 ppm to the same mean transit depth as found in the `CASCADe` analysis for better comparison between the two spectra.

observations were performed in *full imaging* mode, i.e. the snapshot duration was the maximum available time resolution.

Data from *Swift* observations are automatically processed by the *Swift*-project pipeline, and placed in an online publicly-accessible archive. The required data products, all FITS-format files, were downloaded from the archive, on 2023 February 22. These UVOT data products were, for each of the 13 observation segments, the segment image file summed over the snapshots in the segment (1 or 2 in the present case), the snapshot image file containing the individual snapshot images and the detected sources catalogue table. The photometry presented in the images is in units of recorded counts/pixel, where 1 pixel = 1×1 arcsec^2. The ancillary data and visual inspection of the snapshot-level images, indicated that one snapshot (segment-9, snapshot-1) had an aspect-solution problem. These data were excluded from the associated segment image and from further consideration in our analysis, and had been excluded from the automatic pipeline processing. All the following results reported here were based on the segment-level images, i.e. we have available 13 photometry values. We verified that, for the seven segments containing two snaphots, the photometry values were consistent within the statistical errors.

The information in the pipeline-generated source catalogue included, for each detected source, sky-coordinates and photometric values, the latter at successive levels of correction, from 'raw' counts through to PSF-corrected isophotal flux densities. The pipeline source detection employs the *Swift* tool `uvotdetect`, which in turn invokes the SourceExtractor (SE) package [10] to perform source detection and characterisation, including isophotal signal extraction. For WASP-107, we identified, with no ambiguity, the relevant row of the source table based on an estimated epoch=J2023 position using coordinates and proper motions from CDS-SIMBAD. The UV coordinates for all segments lay within 1 arcsec of the estimated optical stellar location and within 0.5 arcsec of the mean UV position. The data were analysed interactively using the *Swift* software tools in `HEASoft` 6.31.1 and the latest available calibration files (CALDB dated 2021-11-08), with ds9 to display the images, and TOPCAT/STILTS [11] to manipulate and view the source-catalogue tables. As recommended by the *Swift* project, we used the `uvotmaghist` tool, with a source-data extraction radius of 5 arcsec centred on the mean UV position, to perform aperture photometry for WASP-107 on the 13 segment images. We used an annular background region with the same centre, and inner and outer radii of 20 and 40 arcsec respectively. We determined by inspection of the UVOT source detections and visually on the images, that the selected background region was free of contamination from nearby sources, and the inner radius was sufficiently removed from the target source to avoid significant contamination.

All 13 aperture-photometry values are consistent within the statistical errors (which dominate the overall errors, as reported by `uvotmaghist`), with a reduced chi-square $\chi^2/\mathrm{dof} \sim 1$ about the mean (with the degrees of freedom, dof, being 12); and at $\sim$10%, the sample standard deviation was comparable with the 1σ error on the individual data values. The source count rate from individual segments was $\sim$0.1$\pm$0.01 ct/s. The mean flux density received at Earth distance was 1.08 ± 0.03 erg cm^{-2} s^{-1} Å^{-1}, corresponding to a luminosity of 5.4 erg s^{-1} Å^{-1} and a flux density incident on WASP-107b of 6.4 erg cm^{-2} s^{-1} Å^{-1}. We found good agreement between the flux values from `uvotmaghist` aperture photometry and uvotdetect/SE isophotal extraction. In making the conversion from instrumental count rate to calibrated flux values, `uvotmaghist` and `uvotdetect` assume a gamma-ray-burst-type spectrum, given the prime objective of the mission. However, the difference for a cool-star spectrum is expected to be no more than $\sim$15% [12]. Given the proximity of WASP-107 to Earth ($\sim$65 pc, and relatively high galactic latitude ($\sim$52 deg), we have not attempted to make any allowance for extinction along the line-of-sight. We note that the NUV irradiance of WASP-107b by its host star is (by chance) comparable (within a factor ~ 2) with that of the Earth by the Sun [13], the larger separation of the latter pair being offset by the Sun's hotter and larger-area photosphere (spectral type G2 V versus K6 V).

3.2. X-ray emission

XMM-Newton has observed the host star WASP-107 on 2018-06-22 (ObsID 0830190901) with the EPIC X-ray telescope (pn, MOS1, MOS2 instruments; all utilising the THIN filter) [14,15] yielding an exposure time of $\sim 60\,\mathrm{ks}$ in a single, continuous observation. The host star was detected in X-rays [16–19], with an X-ray flux in the order of 1×10^{-14} erg cm^{-2} s^{-1} in the soft X-rays, equivalent to a luminosity of $\sim (4-7) \times 10^{27}$ erg s^{-1} (depending on the adopted spectral energy range) for a distance of 64.7 pc, yielding an X-ray flux incident on WASP-107b of $\sim 5 \times 10^2$ erg cm^{-2} s^{-1} [18].

The flux and luminosity values in the cited literature have a wide range with differences of up to $\sim$40%. Therefore, we have performed our own analysis of the XMM-Newton X-ray data, using the SAS data-analysis package, to extract source (and background) counts as a function of photon energy. We binned the spectra to bins with at least 25 source counts each to allow for proper application of χ^2 fit statistics. The source count-rate was $\sim$0.01 ct/s, and the time-series showed no evidence for variability. The XSPEC package [20] was used for fitting optically-thin thermal models in collisional equilibrium (coronal models) to the extracted spectra, having two temperature components representing a wider, presumably continuous distribution of plasma, and a photoelectric absorption component to account for interstellar absorption. The data from all three EPIC instruments were fitted simultaneously after removing the notoriously difficult lowest-energy spectral bins below 0.2 keV. Following ref.[19], we adopted a fixed, interstellar photoelectric absorption component equivalent to a hydrogen column density of $N_{\mathrm{H}} = 2 \times 10^{19}$ cm^{-2} given the distance to WASP-107.

Owing to the relatively modest signal-to-noise ratio (SNR) of the spectrum, the fits converged to two classes of solutions in very different temperature regimes. We discriminated between them by requiring that the solution fulfils the general scaling law between average X-ray stellar surface flux and the logarithmically averaged coronal temperature, using the emission measures (EM $= \int n_e n_i \mathrm{d}V$, where n_e and n_i are the coronal electron and ion number densities, respectively, and V is the coronal volume occupied by the plasma) of the components as weights [21].

The coronal abundances are important quantities for such a fit but the limited SNR does not allow individual element abundances to be retrieved. We therefore used one common abundance factor Z for all elements with respect their solar photospheric values (relative to H). We then stepped through a grid of fixed Z values, fitting the spectrum for each Z, and then searching for a solution that fulfils the coronal flux-temperature scaling relation while providing low χ^2 value. Such a solution exists, with a reduced χ^2 value of 0.94 for $Z = 0.22$. The formal best-fit yielded temperatures of $T_1 = 1.69$ MK (million K) and $T_2 = 8.6$ MK, with an emission-measure ratio $\mathrm{EM}_2/\mathrm{EM}_1 = 0.54$. The EM-weighted logarithmic average of the coronal temperatures as defined in ref.[21] $\left(\log \bar{T} = \sum_i \mathrm{EM}_i \log T_i / \sum_i \mathrm{EM}_i\right)$ is $\bar{T} = 2.96$ MK, a relatively modest temperature as expected for a low-activity star. The corresponding absorption-corrected X-ray flux at Earth in the spectral range of 0.1 – 10 keV is 1.76×10^{-14} erg cm^{-2} s^{-1}, equivalent to a luminosity of $L_{\mathrm{X}} \approx 8.8 \times 10^{27}$ erg s^{-1} for a distance of 64.7 pc, yielding an X-ray flux incident on WASP-107b of $\sim 9.7 \times 10^2$ erg cm^{-2} s^{-1}.

A rotation period of 17.5 ± 1.5 d was derived from *Kepler* K2 photometry [22], while the WASP-107 photometry yields an estimate of 17 ± 1 d [23]. From gyrochronology modelling and the rotation period derived from the WASP photometry, an age estimate of 3.4 ± 0.3 Gyr has been derived [24]. From recent studies of the activity-age-rotation relation for cool main-sequence stars[25] we would expect an X-ray luminosity in the order of 10^{28} erg s^{-1} for a star with a mass of $0.68\ M_{\odot}$ and an age of a few Gyr. This matches our derived X-ray luminosity very well.

4. Corner plots for the `ARCiS` and `petitRADTRANS` retrieval setups.

We here provide the corner plots for the `ARCiS` (Fig. 5) and `petitRADTRANS` (Fig. 6) retrieval setups.

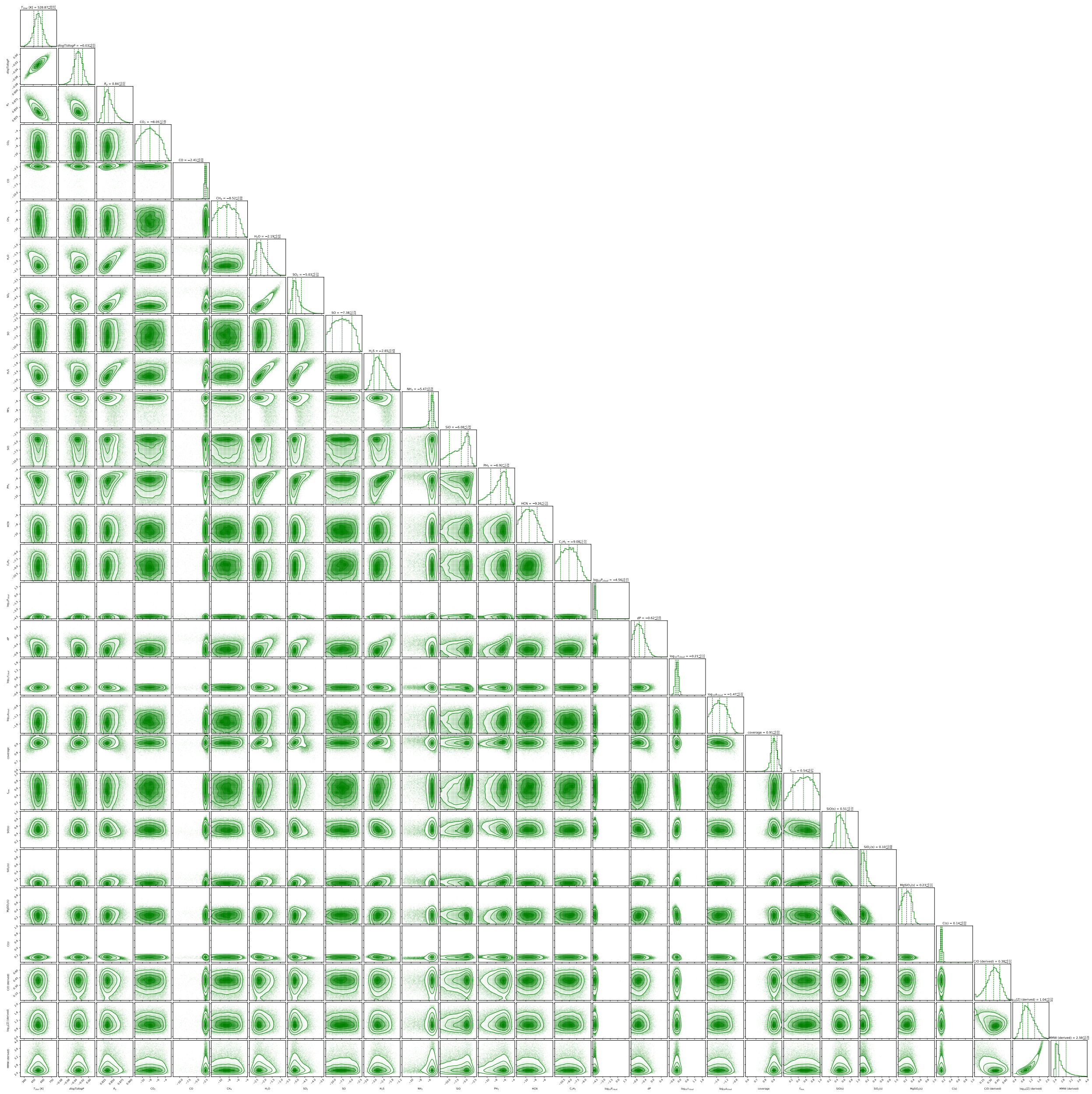

Suppl. Inf. – Figure 5: **Full corner plot for the retrieval of the transit spectrum with the `ARCiS` setup.** The posterior distribution is shown for all retrieval parameters with the addition of the derived parameters metallicity ([Z]), C/O ratio and mean molecular weight (MMW). Gas absorber abundances are shown in logarithms (base 10) of the volume mixing ratios.

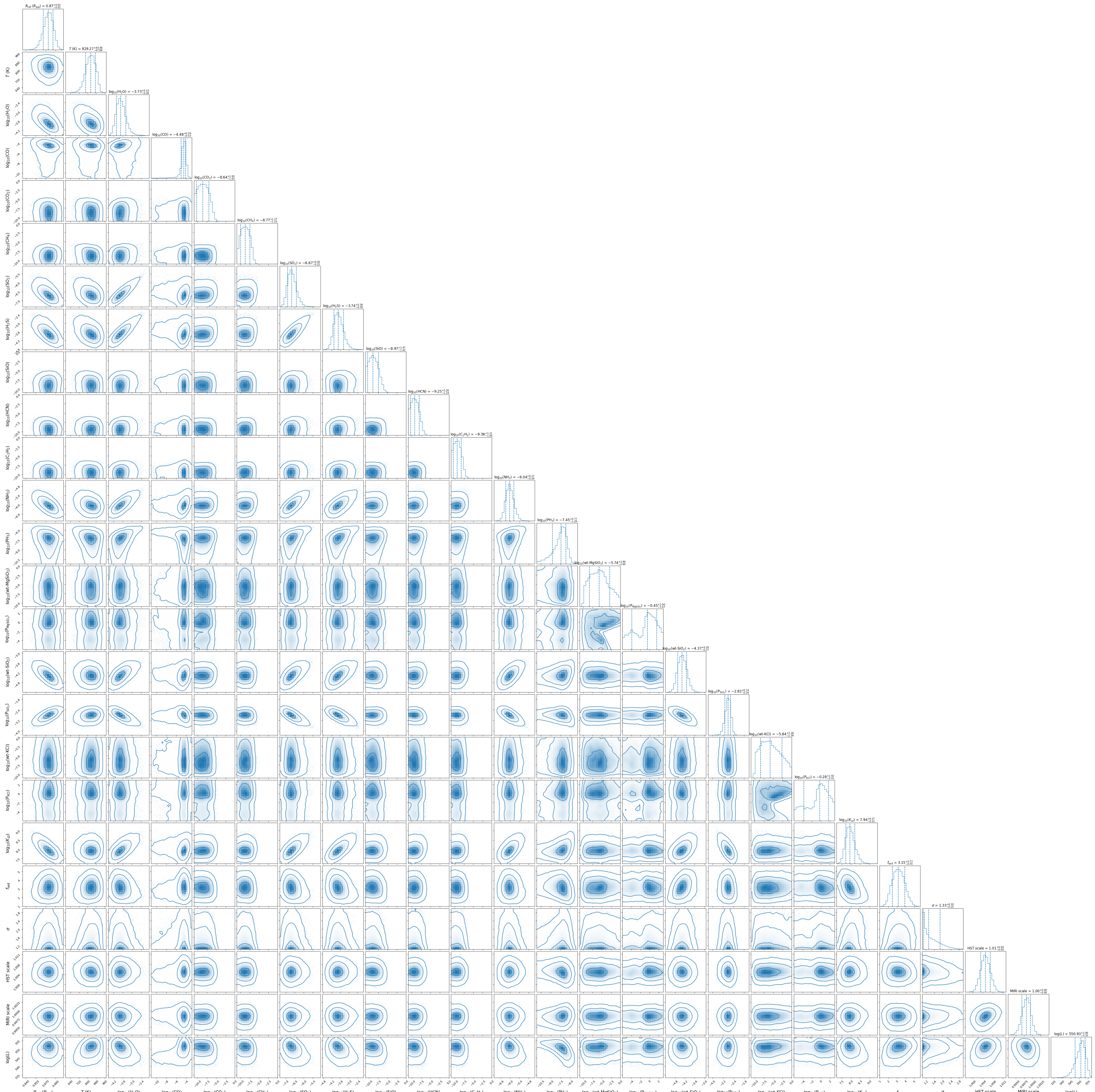

Suppl. Inf. – Figure 6: **Full corner plot for the retrieval of the transit spectrum with the petitRADTRANS setup.** The posterior distribution is shown for all retrieval parameters. Gas absorber abundances are shown in logarithms (base 10) of the volume mixing ratios, while the cloud abundance at the cloud deck is given in log (base 10) mass fractions.

References

1. Ressler, M. E. *et al.* The Mid-Infrared Instrument for the James Webb Space Telescope, VIII: The MIRI Focal Plane System. *Pub. Astron. Soc. Pacific* **127**, 675 (2015).
2. Morrison, J. JWST MIRI flight performance: Detector Effects and Data Reduction Algorithms. *in prep.* (2023).
3. Argyriou, I. *et al.* The Brighter-Fatter Effect in the JWST MIRI Si:As IBC detectors I. Observations, impact on science, and modelling. *arXiv e-prints* arXiv:2303.13517 (2023).
4. Kreidberg, L., Line, M. R., Thorngren, D., Morley, C. V. & Stevenson, K. B. Water, High-altitude Condensates, and Possible Methane Depletion in the Atmosphere of the Warm Super-Neptune WASP-107b. *Astrophys. J. Lett.* **858**, L6 (2018).
5. Carone, L. *et al.* Indications for very high metallicity and absence of methane in the eccentric exo-Saturn WASP-117b. *Astron. Astrophys.* **646**, A168 (2021).
6. Ivshina, E. S. & Winn, J. N. TESS Transit Timing of Hundreds of Hot Jupiters. *Astrophys. J. Suppl.* **259**, 62 (2022).
7. Roming, P. W. A. *et al.* The Swift Ultra-Violet/Optical Telescope. *Space Science Rev.* **120**, 95–142 (2005).
8. Salz, M. *et al.* Swift UVOT near-UV transit observations of WASP-121 b. *Astron. Astrophys.* **623**, A57 (2019).
9. Poole, T. S. *et al.* Photometric calibration of the Swift ultraviolet/optical telescope: Photometric calibration of the Swift UVOT. *Mon. Not. Roy. Astron. Soc.* **383**, 627–645 (2007).
10. Bertin, E. & Arnouts, S. SExtractor: Software for source extraction. *Astron. Astrophys. Suppl.* **117**, 393–404 (1996).
11. Taylor, M. B. TOPCAT & STIL: Starlink Table/VOTable Processing Software. In Shopbell, P., Britton, M. & Ebert, R. (eds.) *Astronomical Data Analysis Software and Systems XIV*, vol. 347 of *Astron. Soc. Pacific Conf. Series*, 29 (2005).
12. Breeveld, A. A. *et al.* An Updated Ultraviolet Calibration for the Swift/UVOT. In McEnery, J. E., Racusin, J. L. & Gehrels, N. (eds.) *Gamma Ray Bursts 2010*, vol. 1358 of *American Institute of Physics Conference Series*, 373–376 (2011).
13. Woods, T. N. *et al.* Solar Irradiance Reference Spectra (SIRS) for the 2008 Whole Heliosphere Interval (WHI). *Geophys. Res. Lett.* **36**, L01101 (2009).
14. Strüder, L. *et al.* The European Photon Imaging Camera on XMM-Newton: The pn-CCD camera. *Astron. Astrophys.* **365**, L18–L26 (2001).

15. Turner, M. J. L. *et al.* The European Photon Imaging Camera on XMM-Newton: The MOS cameras. *Astron. Astrophys.* **365**, L27–L35 (2001).

16. Webb, N. A. *et al.* The *XMM-Newton* serendipitous survey: IX. The fourth *XMM-Newton* serendipitous source catalogue. *Astron. Astrophys.* **641**, A136 (2020).

17. Nortmann, L. *et al.* Ground-based detection of an extended helium atmosphere in the Saturn-mass exoplanet WASP-69b. *Science* **362**, 1388–1391 (2018).

18. Foster, G., Poppenhaeger, K., Ilic, N. & Schwope, A. Exoplanet X-ray irradiation and evaporation rates with eROSITA. *Astron. Astrophys.* **661**, A23 (2022).

19. Spinelli, R. *et al.* Planetary Parameters, XUV Environments, and Mass-loss Rates for Nearby Gaseous Planets with X-Ray-detected Host Stars. *Astron. J.* **165**, 200 (2023).

20. Arnaud, K. A. XSPEC: The First Ten Years. In Jacoby, G. H. & Barnes, J. (eds.) *Astronomical Data Analysis Software and Systems V*, vol. 101 of *Astron. Soc. Pacific Conf. Series*, 17 (1996).

21. Johnstone, C. P. & Güdel, M. The coronal temperatures of low-mass main-sequence stars. *Astron. Astrophys.* **578**, A129 (2015).

22. Močnik, T., Hellier, C., Anderson, D. R., Clark, B. J. M. & Southworth, J. Starspots on WASP-107 and pulsations of WASP-118. *Mon. Not. Roy. Astron. Soc.* **469**, 1622–1629 (2017).

23. Anderson, D. R., Collier Cameron, A. & Delrez, L. The discoveries of WASP-91b, WASP-105b and WASP-107b: Two warm Jupiters and a planet in the transition region between ice giants and gas giants. *Astron. Astrophys.* **604**, A110 (2017).

24. Piaulet, C. *et al.* WASP-107b's Density Is Even Lower: A Case Study for the Physics of Planetary Gas Envelope Accretion and Orbital Migration. *Astron. J.* **161**, 70 (2021).

25. Johnstone, C. P., Bartel, M. & Güdel, M. The active lives of stars: A complete description of the rotation and XUV evolution of F, G, K, and M dwarfs. *Astron. Astrophys.* **649**, A96 (2021).